

Learnable Retrieval Enhanced Visual-Text Alignment and Fusion for Radiology Report Generation

Qin Zhou^{1,2,*}, Guoyan Liang^{3,4,*}, Xindi Li^{3,4}, Jingyuan Chen³, Wang Zhe^{1,2,†}, Chang Yao^{3,4,†}, Sai Wu^{3,4,†}

¹Department of Computer Science and Engineering, ECUST, China

²Key Laboratory of Smart Manufacturing in Energy Chemical Process, Ministry of Education, P. R. China

³Zhejiang University, Hangzhou, China

⁴Hangzhou High-Tech Zone (Binjiang) Institute of Blockchain and Data Security

{sunniezq, wangzhe}@ecust.edu.cn, {guoyanl, 12421143, jingyuanchen, changy, wusai}@zju.edu.cn

Abstract

Automated radiology report generation is essential for improving diagnostic efficiency and reducing the workload of medical professionals. However, existing methods face significant challenges, such as disease class imbalance and insufficient cross-modal fusion. To address these issues, we propose the learnable Retrieval Enhanced Visual-Text Alignment and Fusion (REVTAF) framework, which effectively tackles both class imbalance and visual-text fusion in report generation. REVTAF incorporates two core components: (1) a Learnable Retrieval Enhancer (LRE) that utilizes semantic hierarchies from hyperbolic space and intra-batch context through a ranking-based metric. LRE adaptively retrieves the most relevant reference reports, enhancing image representations, particularly for underrepresented (tail) class inputs; and (2) a fine-grained visual-text alignment and fusion strategy that ensures consistency across multi-source cross-attention maps for precise alignment. This component further employs an optimal transport-based cross-attention mechanism to dynamically integrate task-relevant textual knowledge for improved report generation. By combining adaptive retrieval with multi-source alignment and fusion, REVTAF achieves fine-grained visual-text integration under weak image-report level supervision while effectively mitigating data imbalance issues. The experiments demonstrate that REVTAF outperforms state-of-the-art methods, achieving an average improvement of 7.4% on the MIMIC-CXR dataset and 2.9% on the IU X-Ray dataset. Comparisons with mainstream multimodal LLMs (e.g., GPT-series models), further highlight its superiority in radiology report generation¹.

1. Introduction

Radiology reports are crucial for clinical diagnosis and treatment, but manual generation is time-consuming and heavily dependent on radiologists' expertise, often leading to delays and inconsistencies in medical decision-making. Traditional methods typically view report generation as an extension of image captioning [6, 24, 32, 41, 43]. However, unlike image captioning, which assigns equal weight to all visual concepts, radiology reports must prioritize abnormal findings. These findings are often subtle and imbalanced compared to normal details, causing models to overlook critical diagnostic cues [12]. Furthermore, radiologists typically generate reports sentence-by-sentence, each describing an imaging pattern based on regional abnormal findings, which is not originally provided in the training data. The lack of detailed region-sentence correspondence in the training set, leading to insufficient visual-text alignment and fusion during report generation. Recent methods have attempted to address these challenges by incorporating external knowledge through auxiliary tasks like classification or by integrating reference reports via retrieval-based algorithms [13, 16, 18]. However, these strategies often fail to provide precise reference information and neglect fine-grained visual-text alignment, potentially introducing irrelevant or incorrect knowledge and further compromising the quality of visual-text integration.

To address these issues, we propose the learnable Retrieval Enhanced Visual-Text Alignment and Fusion (REVTAF) framework. Specifically, we introduce a Learnable Retrieval Enhancer (LRE) module that dynamically retrieves the most relevant reference reports for each input image, acting as Global Reference Prompts (GRPs). This enhances the visual representation, particularly for tail classes, which require precise reference information. In LRE, we map visual features into the hyperbolic space to utilize the semantic hierarchy of images and develop a ranking-based

*These authors contributed equally.

†Corresponding Authors.

¹<https://github.com/banbooliang/REVTAF-RRG>

metric to explore intra-batch contextual relationships. We use the hashing distance between multi-class disease labels as a strong supervisory signal to guide the metric learning process.

To improve cross-modal information integration under weak image-report level supervision, we propose a novel Fine-grained Visual-Text Alignment and Fusion (FVTAF) module. This module introduces a Fine-grained Cross-modal Consistency (FCC) constraint that aligns visual and text data using semantic similarities between multi-source text prompts (i.e., GRPs and LRPs). The report-level Global Reference Prompts (GRPs) are generated by the above-mentioned LRE module, while entity-specific Local Reference Prompts (LRPs) are derived from the MedKLIP foundation model [35]. Additionally, we incorporate the optimal transport-based cross-attention mechanism to extract relevant information from the multi-source text prompts, ensuring thorough feature fusion.

Our main contributions are outlined as follows:

- We propose a novel framework that combines a Learnable Retrieval Enhancer and a Fine-grained Visual-Text Alignment and Fusion module to simultaneously tackle the challenges of class imbalance and insufficient cross-modal fusion.
- We pioneer a learnable solution for adaptively retrieving the most relevant reference report for each input image, effectively augmenting the representation of visual input, particularly for tail classes.
- We design a novel visual-text alignment and fusion module that integrates Fine-grained Cross-modal Consistency with an optimized cross-attention mechanism, enabling more effective visual-text integration.
- Extensive comparisons with state-of-the-art radiology report generation methods and multimodal LLMs, as well as ablative studies, consistently demonstrate the superior performance of our approach.

2. Related Work

2.1. Image Captioning

Generating radiology reports shares many similarities with the image captioning task, which focuses on producing concise textual descriptions of images, and has garnered significant research interest in recent years [1, 20, 24, 34]. Most approaches in image caption rely on an encoder-decoder framework: an image encoder first extracts visual features, which are then passed to a text decoder to generate the final captions. Early studies [1, 14, 20] primarily employed Long Short-Term Memory (LSTM) networks [9] and Convolutional Neural Networks (CNN) [23] to tackle this task. Recently, transformer models that leverage attention mechanisms [29] have become prevalent due to their superior capability in processing intricate vision and language features

[6, 24, 34]. Additionally, innovative training strategies such as reinforcement learning [26] and adversarial training [7] have further boosted performance in image captioning. Recent advancements in foundation models have highlighted the effectiveness of large-scale visual-language pre-training [10, 33, 41] for image captioning tasks. However, these methods often fail to incorporate domain-specific medical knowledge and lack region-to-sentence level correspondence, which significantly limits their applicability to radiology report generation [34].

2.2. Radiology Report Generation

Radiology reports typically comprise multiple descriptive sentences that detail the findings observed in radiological images. Unlike standard image captioning tasks, radiology report generation requires not only producing longer outputs but also achieving greater precision in describing region-specific imaging findings. To tackle these challenges, various methods have been proposed [4, 11, 13, 15, 36].

Some works leverage memory-based approaches to capture and retain critical information. For instance, R2Gen [4] and R2GenCMN [5] enhance the standard encoder-decoder framework by separately fusing image and caption data using LSTM and cross-modal memory networks (CMN). These models utilize shared memory to record the alignment between images and text, thereby facilitating effective cross-modal interactions. Inspired by this idea, XproNet [31] employs a shared cross-modal prototype matrix that serves as external knowledge, capturing and embedding cross-modal prototypes to improve report generation.

Other approaches integrate additional knowledge sources to assist the generation process. Clinical-BERT [36] introduces a visual-language pre-trained model that incorporates medical domain knowledge to boost performance. Similarly, [18] explores the integration of both posterior and prior knowledge distilled from visual cues, medical graphs, and retrieved reports. PromptMRG [13] incorporates auxiliary multi-disease classification task to improve diagnostic accuracy. Some approaches focus on modeling relational context across text or key visual information to enhance the report generation. The DCL model [15] fuses information from a pre-constructed knowledge graph that encodes relationships between caption words, while KiUT [11] introduces a knowledge-injected U-transformer that learns multi-level visual representations and adaptively distills contextual and clinical knowledge for precise word prediction. EKAGen [2] converts expert reports into an embedding space to prevent the loss of salient features and to enhance focus on key regions. Despite progress, current methods still face challenges in *balancing disease categories and effectively integrating visual-text data, limiting radiology report quality.*

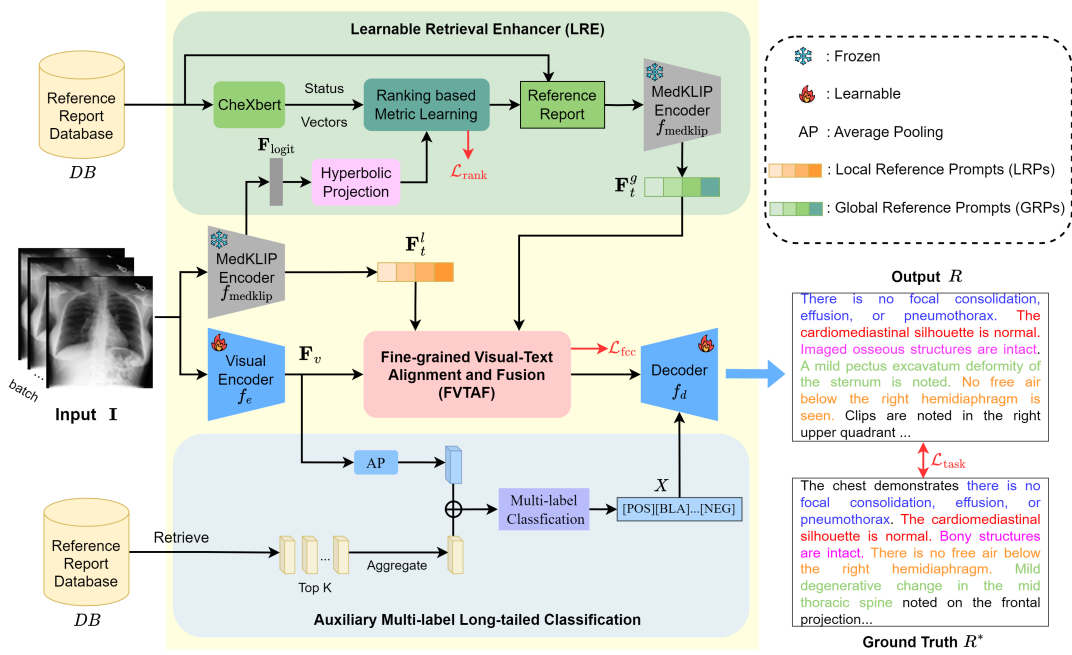


Figure 1. Overview of the proposed Retrieval Enhanced Visual-Text Alignment and Fusion (REVTAF) framework.

3. Method

This section delves into the specifics of our learnable Retrieval Enhanced Visual-Text Alignment and Fusion (REVTAF) framework. Initially, we will introduce the essential background on radiology report generation to provide context for our approach.

3.1. Preliminaries

Radiology report generation refers to automatically generating structured and coherent radiology reports from medical imaging data. Formally, given a 2D radiology image I , the model is tasked with interpreting the image and generating a descriptive radiology report $R = \{r_1, r_2, \dots, r_T\}$, where T is the length of the report, and \mathbb{V} represents the vocabulary, each $r_t \in \mathbb{V}$ is a token. The entire recursive generation process is formulated as follows,

$$p(R|I) = \prod_{t=1}^T p(r_t|r_1, \dots, r_{t-1}, I). \quad (1)$$

The report generation process is optimized by minimizing the cross-entropy loss,

$$\mathcal{L}_{task} = -\sum_{t=1}^T \log(p(r_t|r_{1:t-1})). \quad (2)$$

Existing approaches [3, 13] for radiology report generation use pre-trained models (e.g., CLIP) to compute similarity scores between an image and training reports, retrieving the most relevant report to guide the generation process.

However, these methods face several challenges. First, the absence of domain-specific knowledge in pre-trained models often leads to suboptimal reference selection. Second, imbalanced disease labels result in biased reports that neglect rare diseases and subtle anomalies. Additionally, the lack of fine-grained alignment hinders effective visual-text feature fusion under weak image-report level supervision. Our proposed REVTAF framework effectively addresses the aforementioned challenges, establishing a new benchmark for the community.

3.2. Framework Overview

Figure 1 outlines the workflow of our REVTAF framework. Given an input image $I \in \mathbb{R}^{H \times W}$ and a reference report database $DB = \{R_1, \dots, R_{N_D}\}$, where N_D is the number of reference reports in the database, REVTAF employs an encoder-decoder architecture for radiology report generation. The visual encoder f_e extracts intermediate features $F_v \in \mathbb{R}^{H_v \times W_v \times d_v} = f_e(I)$, while the text decoder f_d generates the final report. To enhance cross-modal alignment, we introduce two components:

(1) entity-specific Local Reference Prompts (LRPs): We adopt the pre-trained MedKLIP model to produce local text prompts $F_t^l \in \mathbb{R}^{M \times d_l}$, where M corresponds to refined entity classes as described in [42].

(2) report-level Global Reference Prompts (GRPs): A Learnable Retrieval Enhancer (LRE) adaptively retrieves the most relevant report from DB by learning a hyperbolic space ranking metric that captures image semantic hierar-

chies and intra-batch context. Denote R_{ref} as the retrieved most relevant report. Then we generate the corresponding report-level GRPs as $\mathbf{F}_t^g \in \mathbb{R}^{N \times d_g} = f_{medklip}(R_{ref})$, with N denoting the maximum sentence count in DB , $f_{medklip}$ representing the pretrained MedKLIP encoder.

The Fine-grained Visual-Text Alignment and Fusion (FVTAF) module integrates multi-source prompts (\mathbf{F}_t^l and \mathbf{F}_t^g) with visual features \mathbf{F}_v . It introduces a novel Fine-grained Cross-modal Consistency constraint for visual-text alignment, alongside an optimal transport-based cross-attention mechanism to fuse $\{\mathbf{F}_v, \mathbf{F}_t^g\}$ into global cross-modal features \mathbf{F}_c^g . Similarly, local cross-modal features \mathbf{F}_c^l are generated from $\{\mathbf{F}_v, \mathbf{F}_t^l\}$. Following [13], an auxiliary multi-label long-tailed classification branch produces disease-related prompts X to mitigate data imbalance. Finally, the decoder f_d synthesizes the fused visual-text features $\mathbf{F}_c = \oplus(\mathbf{F}_c^g, \mathbf{F}_c^l)$ (where $\oplus(\cdot)$ denotes concatenation along the feature dimension) and X to generate the final report $R = f_d(\mathbf{F}_c, X)$. Details of the proposed LRE and FVTAF modules are discussed in subsequent sections.

3.3. Learnable Retrieval Enhancer

The relevance of the retrieved reference report is crucial for effective guidance, particularly in cases of long-tailed distribution [13]. Current methods [3, 13] rely on reports linked to database images with similar pooled CLIP features for reference. However, this approach lacks medical domain knowledge and overlooks important spatial details. To address these issues, we propose the Learnable Retrieval Enhancer (LRE) to enhance retrieval relevance.

First, we leverage the medical foundation model MedKLIP to extract visual features from training images and text features from reports. MedKLIP generates entity-specific logits $\mathbf{F}_{logit} \in \mathbb{R}^{B \times M}$ (where B = batch size, M = 75 entity classes), highlighting abnormal findings in input images. Building on this, we design a hyperbolic space ranking-based metric to learn hierarchical visual similarities among training images within current mini-batch, supervised by hashing distances derived from disease labels related to the corresponding reports.

Hyperbolic Space Distance. Given the remarkable structural consistency of medical images, where each organ exhibits a well-defined spatial arrangement, we project entity-specific logits \mathbf{F}_{logit} into hyperbolic space using a Hyperbolic Neural Network (HNN) [39]. HNN can adaptively learn hierarchical representations tailored to anatomical organization. Let the resulting hyperbolic features be denoted as $\mathbf{H} \in \mathbb{R}^{B \times d_h} = \text{HNN}(\mathbf{F}_{logit})$, where d_h is the hyperbolic embedding dimension. In the Poincaré ball model with curvature c (\mathbb{B}^c), the geodesic distance $d_{\mathbb{B}}^c(\mathbf{x}, \mathbf{y})$ between two points $\mathbf{x}, \mathbf{y} \in \mathbb{B}^c$ is computed as:

$$d_{\mathbb{B}}^c(\mathbf{x}, \mathbf{y}) = \frac{2}{\sqrt{c}} \tanh^{-1}(\sqrt{c} \|\mathbf{x} \oplus_c \mathbf{y}\|), \quad (3)$$

where \oplus_c denotes the Möbius addition operation:

$$\mathbf{x} \oplus_c \mathbf{y} = \frac{(1 + 2c\mathbf{x}^\top \mathbf{y} + c\|\mathbf{y}\|^2)\mathbf{x} + (1 - c\|\mathbf{x}\|^2)\mathbf{y}}{1 + 2c\mathbf{x}^\top \mathbf{y} + c^2\|\mathbf{x}\|^2\|\mathbf{y}\|^2}. \quad (4)$$

Using Eq. (3), we compute the pairwise distance matrix $\hat{D} \in \mathbb{R}^{B \times B} = \{\hat{D}_{ij}, i, j \in 1, \dots, B\}$ for the entire batch, where each element \hat{D}_{ij} represents the hyperbolic distance between samples i and j . Let \mathbf{h}_i and \mathbf{h}_j denote the hyperbolic features of the i -th and j -th samples in current batch. Then \hat{D}_{ij} is computed as,

$$\hat{D}_{ij} = d_{\mathbb{B}}^c(\mathbf{h}_i, \mathbf{h}_j). \quad (5)$$

To incorporate semantic guidance into hyperbolic feature learning, we leverage the semantic similarity between paired radiology reports as supervisory signal. Specifically, for each sample, we extract structured classification labels from its corresponding report R using CheXbert [27], which maps R to $K = 18$ predefined disease categories. Each category is assigned one of four statuses: Blank (unmentioned), Positive (disease present), Negative (disease absent), or Uncertain. This results in a 72-dimensional status vector per report, with each element in $\{0, 1\}$. Then we can calculate the ground-truth semantic distance matrix $D \in \mathbb{R}^{B \times B}$ using hashing distance between their status vectors. Let $\mathbf{v}_i, \mathbf{v}_j \in \{0, 1\}^{72}$ denote the status vectors for the i -th and j -th samples, respectively, their semantic distance D_{ij} can be calculated as,

$$D_{ij} = \sum_{k=1}^{72} \mathbb{1}[\mathbf{v}_{i,k} \neq \mathbf{v}_{j,k}], \quad (6)$$

where $\mathbb{1}[\cdot]$ is the indicator function that evaluates to 1 when the inside condition is true, and 0 otherwise. $\mathbf{v}_{i,k}, \mathbf{v}_{j,k}$ denote the k -th values in \mathbf{v}_i and \mathbf{v}_j , respectively.

Ranking based Metric Learning. While a naive approach would compute the Euclidean distance between the hyperbolic distance matrix \hat{D} and the ground-truth pairwise semantic distance matrix D , this method ignores contextual relationships across samples and is prone to outlier sensitivity. To address this, we adopt ranking-based metric learning as follows: For each row of the ground-truth distance matrix D , we sort the entries in ascending order. Denote π_i as the index with the smallest hamming distance relative to the i -th sample within the batch, we then compute a cross-entropy loss by treating the hyperbolic distance matrix \hat{D} as predictions and the ground-truth index vector $\Pi = \{\pi_i\}$ as targets:

$$\mathcal{L}_{\text{rank}} = \text{CE}(\hat{D}, \Pi), \quad (7)$$

where $\text{CE}(\cdot)$ denotes the CrossEntropy loss, penalizing deviations between the predicted hyperbolic distance rankings and the semantic similarity rankings. Note that diagonal values are omitted before ranking to prevent self-comparison. During training, ground-truth hashing distances between reports are used to select the most relevant

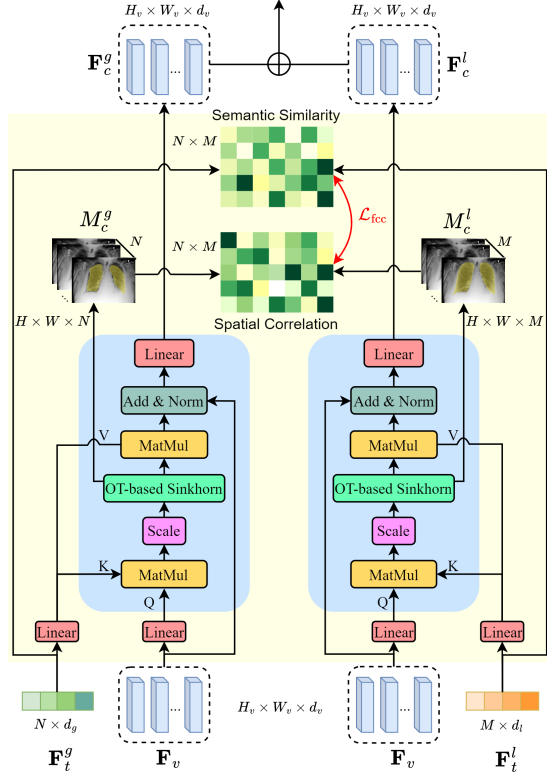


Figure 2. Illustration of the Fine-grained Visual-Text Alignment and Fusion (FVTAF) module.

report as the Global Reference Prompts (GRPs). During inference, the report related to the most similar database image in the learned hyperbolic space is retrieved, generating the report-level GRPs. GRPs then serve as a text input for the subsequent alignment and fusion module.

3.4. Fine-grained Visual-Text Alignment and Fusion

The image-report level weak supervision in medical report generation hinders fine-grained region-sentence alignment. To address this, we propose the Fine-grained Visual-Text Alignment and Fusion (FVTAF) module, which enhances visual input by integrating knowledge from multi-source text inputs, as shown in Figure 2. In addition to the Global Reference Prompts (GRPs) generated above to capture report-level information from the most similar reference image, we introduce entity-specific Local Reference Prompts (LRPs). These LRPs describe disease findings tied to regional imaging patterns within the input image. Specifically, we leverage the MedKLIP foundation model to generate triplets encoding the position and existence of $M = 75$ predefined entities. Formally, each report is represented as a set of triplets:

$$R = \{(entity_m, position_m, exist_m)\}_{m=1}^M, \quad (8)$$

where each triplet for the m -th entity is concatenated and fed into the MedKLIP textual encoder to produce the corresponding local reference prompt. The overall entity-specific LRPs are constructed by concatenating textual embeddings from all entities: $\mathbf{F}_t^l = [\mathbf{F}_t^l(1), \mathbf{F}_t^l(2), \dots, \mathbf{F}_t^l(M)]$, where each $\mathbf{F}_t^l(m)$ is computed as:

$$\mathbf{F}_t^l(m) = f_{\text{medklip}}([entity_m, position_m, exist_m]). \quad (9)$$

Multi-source Cross-modal Fusion. Given the visual features \mathbf{F}_v , report-level Global Reference Prompts (GRPs) \mathbf{F}_t^g and entity-specific Local Reference Prompts (LRPs) \mathbf{F}_t^l , we introduce two visual-text cross-attention branches to enhance the query visual features with knowledge from both GRPs and LRPs. During the visual-text cross attention modeling, instead of adopting the traditional cross-attention mechanism [19, 32], we resort to [40] to utilize the Multi-Prompts Sinkhorn Attention (MPSA) to better incorporate textual knowledge more relevant to the visual embeddings. The MPSA mechanism leverages optimal transport theory to reweight query-key cross-attention with global context, effectively extracting relevant knowledge and filtering out unrelated textual information to better adapt to the input image. For details of the MPSA mechanism, please refer to [40]. Formally, the fused global visual-text features and cross-attention maps can be obtained as,

$$\begin{aligned} \mathbf{F}_c^g, M_c^g &= MPSA(\mathbf{Q}\mathbf{K}^T)\mathbf{V}, \\ \mathbf{Q} &= \phi_q(\mathbf{F}_v), \mathbf{K} = \phi_k(\mathbf{F}_t^g), \mathbf{V} = \phi_v(\mathbf{F}_t^g), \end{aligned} \quad (10)$$

Similarly, we can generate the fused local visual-text features and attention maps as \mathbf{F}_c^l, M_c^l .

To ensure the generated report remains faithful to the input image, we introduce residual connections to retain the original visual features in the fused representations. Specifically, for both global (\mathbf{F}_c^g) and local (\mathbf{F}_c^l) cross-modal features, the final fused features are computed as:

$$\begin{aligned} \mathbf{F}_c^g &= f_{proj}(\text{LayerNorm}(\mathbf{F}_c^g + \mathbf{F}_v)), \\ \mathbf{F}_c^l &= f_{proj}(\text{LayerNorm}(\mathbf{F}_c^l + \mathbf{F}_v)), \end{aligned} \quad (11)$$

where $\text{LayerNorm}(\cdot)$ denotes layer normalization to stabilize training, and f_{proj} is a learnable linear projection layer. The global and local fused features \mathbf{F}_c^g and \mathbf{F}_c^l are then concatenated along the feature dimension to form the final fused representation \mathbf{F}_c , which is passed to the transformer decoder for report generation.

Fine-grained Cross-modal Consistency. To mitigate the impact of irrelevant or incorrect descriptions in Global Reference Prompts (GRPs) and Local Reference Prompts (LRPs), we propose the Fine-grained Cross-modal Consistency (FCC) constraint. This constraint is motivated by the assumption that multi-source text prompts sharing similar semantics should produce correlated responses in their

Model	Year	NLG Metrics						CE Metrics			Avg
		BLEU-1	BLEU-2	BLEU-3	BLEU-4	METEOR	ROUGE	Precision	Recall	F1	
R2Gen	ACL 2020	0.353	0.218	0.145	0.103	0.142	0.277	0.333	0.273	0.276	0.236
M2TR	ACL 2021	0.378	0.232	0.154	0.107	0.145	0.272	0.240	0.428	0.308	0.252
MKSG	MIA 2022	0.363	0.228	0.156	0.115	-	0.284	0.458	0.348	0.371	-
M2KT	MIA 2023	0.386	0.237	0.157	0.111	-	0.274	0.420	0.339	0.352	-
ME	CVPR 2023	0.386	0.250	0.169	0.124	0.152	0.291	0.364	0.309	0.311	0.262
KiUT	CVPR 2023	0.393	0.243	0.159	0.113	0.160	0.285	0.371	0.318	0.321	0.263
DCL	CVPR 2023	-	-	-	0.109	0.150	0.284	0.471	0.352	0.373	-
UAR	ICCV 2023	0.363	0.229	0.158	0.107	0.157	0.289	-	-	-	-
HERGen	ECCV 2024	0.395	0.248	0.169	0.122	0.156	0.285	0.415	0.301	0.317	0.268
CVT2Dis.	Artif.Intell.Med 2022	0.392	0.245	0.169	0.124	0.153	0.285	0.356	0.412	0.384	0.280
CliBert	AAAI 2022	0.383	0.230	0.151	0.106	0.144	0.275	0.397	0.435	0.415	0.282
RGRG	CVPR 2023	0.373	0.249	0.175	0.126	0.168	0.264	0.461	0.475	0.447	0.304
PromptMRG	AAAI 2024	0.398	0.239	0.156	0.112	0.157	0.268	0.501	0.509	0.476	0.313
EKAGen	CVPR 2024	0.419	0.258	0.170	0.119	0.157	0.287	0.517	0.483	0.499	0.323
Ours	-	0.465	0.318	0.235	0.182	0.199	0.336	0.628	0.613	0.592	0.397

Table 1. Comparison with other SOTA methods on the MIMIC-CXR dataset. The best results are highlighted in bold.

cross-modal attention maps (M_c^g and M_c^l). Given global text features \mathbf{F}_t^g (from GRPs) and local text features \mathbf{F}_t^l (from LRPs), we compute a sentence-level semantic similarity matrix $S \in \mathbb{R}^{N \times M}$. Here, S_{nm} represents the cosine similarity between the n -th sentence in GRPs and the m -th entity in LRPs:

$$S_{nm} = \frac{\langle \mathbf{F}_t^g(n), \mathbf{F}_t^l(m) \rangle}{\|\mathbf{F}_t^g(n)\|_2 \|\mathbf{F}_t^l(m)\|_2}, \quad (12)$$

where $\mathbf{F}_t^g(n)$ and $\mathbf{F}_t^l(m)$ denote the n -th sentence and m -th entity embeddings in \mathbf{F}_t^g and \mathbf{F}_t^l , respectively. The similarity matrix S is normalized to the $[0, 1]$ range via a sigmoid function to ensure stable alignment.

We quantify the spatial correlation of cross-attention maps M_c^g (as calculated in Eq. 10) and M_c^l using Intersection-over-Union (IoU). For the n -th attention map $M_c^g(n)$ in M_c^g and the m -th map $M_c^l(m)$ in M_c^l , their spatial overlap O_{nm} is computed as:

$$O_{nm} = \text{IoU} (M_c^g(n), M_c^l(m)), \quad (13)$$

$$= \frac{\sum (M_c^g(n) \cap M_c^l(m))}{\sum (M_c^g(n) \cup M_c^l(m))},$$

where \cap and \cup denote element-wise minimum and maximum operations, respectively. The FCC loss (\mathcal{L}_{fcc}) penalizes discrepancies between semantic similarity (S) and spatial correlation (O):

$$\mathcal{L}_{\text{fcc}} = \frac{1}{N \times M} \sum_{n=1}^N \sum_{m=1}^M (1 - S_{nm} \cdot O_{nm}), \quad (14)$$

The overall training objective \mathcal{L} is the combination of $\mathcal{L}_{\text{task}}$, $\mathcal{L}_{\text{rank}}$, and \mathcal{L}_{fcc} ,

$$\mathcal{L} = \mathcal{L}_{\text{task}} + \alpha \mathcal{L}_{\text{rank}} + \beta \mathcal{L}_{\text{fcc}}, \quad (15)$$

where α and β are balancing coefficients.

4. Experiments

In this section, we demonstrate the effectiveness of our REVTAf framework through comprehensive comparisons. Owing to space constraints, we present further ablation experiments in the [supplementary material](#).

4.1. Experimental Setups

Datasets and Evaluation Metrics. We evaluate our model on two widely used radiology report generation benchmarks: MIMIC-CXR and IU X-Ray. The MIMIC-CXR dataset, provided by the Beth Israel Deaconess Medical Center, contains a large-scale collection of chest X-ray images paired with corresponding reports. Following prior studies [5, 11, 13], we split the dataset into 270,790 training samples, 2,130 validation samples, and 3,858 test samples for fair comparison. The IU X-Ray dataset from Indiana University includes 7,470 frontal and lateral chest X-ray images and 3,955 associated reports. Due to the limited positive samples for certain diseases in the test set of the offline split [13], we follow previous methods to evaluate the model trained on MIMIC-CXR, directly on the entire IU X-Ray dataset.

Our model’s performance is assessed in two aspects: natural language generation (NLG) and clinical efficacy (CE). For NLG, we measure report quality using BLEU [25], METEOR [8], and ROUGE-L [17]. For CE, we use CheXbert [12] to annotate generated reports and compare them with ground truth labels across 14 categories, evaluating precision, recall, and F1 score.

Implementation Details. We adopt a ResNet-101 model pre-trained on ImageNet as the image encoder. And the MedKLIP model [35] pre-trained on a widely used radiology report dataset is leveraged as the text encoder, initially

Model	Year	NLG Metrics						CE Metrics			Avg
		BLEU-1	BLEU-2	BLEU-3	BLEU-4	METEOR	ROUGE	Precision	Recall	F1	
R2Gen	ACL 2020	0.289	0.155	0.087	0.052	0.128	0.243	0.151	0.145	0.145	0.155
M2KT	MIA 2023	0.371	0.239	0.151	0.078	0.153	0.261	0.153	0.145	0.145	0.188
DCL	CVPR 2023	0.354	0.230	0.148	0.074	0.152	0.267	0.168	0.167	0.162	0.191
RGRG	CVPR 2023	0.266	0.215	0.147	0.063	0.146	0.180	0.183	0.187	0.180	0.174
CVT2Dis.	Artif.Intell.Med 2022	0.383	0.236	0.157	0.082	0.147	0.277	0.174	0.172	0.168	0.200
PromptMRG	AAAI 2024	0.401	0.247	0.160	0.098	0.160	0.281	0.213	0.229	0.211	0.222
Ours	-	0.420	0.249	0.159	0.107	0.176	0.309	0.286	0.282	0.273	0.251

Table 2. Comparing the performance of our model with other SOTA methods on the IU X-Ray dataset.

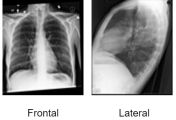

Input	PromptMRG	Baseline	Ours	Ground Truth
 Frontal Lateral	There is no focal consolidation effusion or pneumothorax. The cardiomeastinal silhouette is normal. Imaged osseous structures are intact. No free air below the right hemidiaphragm is seen.	The lungs are well expanded and clear. Cardiomeastinal and hilar contours are unremarkable. There is no pleural effusion or pneumothorax. Clips are noted in the right upper quadrant of the abdomen. No subdiaphragmatic free air is present. Osseous structures are grossly intact. There is no free air under the diaphragm.	The lungs are well inflated and clear. The cardiomeastinal silhouette and hilar contours and pleural surfaces are normal. There is no pleural effusion or pneumothorax. Surgical clips in the right upper quadrant suggest prior cholecystectomy. No acute osseous abnormality is identified. There is no free air under the diaphragm.	The cardiac, mediastinal, and hilar contours are normal. Pulmonary vascularity is normal, and the lungs are clear. No pleural effusion or pneumothorax is present. There are no acute osseous abnormalities. Clips are noted within the upper abdomen compatible with prior cholecystectomy.
 Frontal Lateral	The lung volumes are low. The cardiac, mediastinal and hilar contours appear within normal limits. There is no pleural effusion or pneumothorax. There is mild elevation of the right hemidiaphragm. The lungs appear clear. Mild degenerative changes are similar along the mid thoracic spine. There has been no significant change allowing for differences in technique.	Lung volumes are low. Left - sided dual - chamber pacemaker device is noted with leads terminating in the right atrium and right ventricle. Mild enlargement of the cardiac silhouette is present. The mediastinal and hilar contours are unremarkable. Pulmonary vasculature is not engorged. No focal consolidation, pleural effusion or pneumothorax is present. There are no acute osseous abnormalities.	Lung volumes are low. Left - sided dual - chamber pacemaker device is noted with leads terminating in the right atrium and right ventricle. Heart size is mildly enlarged. Mediastinal and hilar contours are unremarkable. Crowding of bronchovascular structures is present without overt pulmonary edema. Patchy opacities in the lung bases likely reflect areas of atelectasis. No pleural effusion or pneumothorax is present. There are no acute osseous abnormalities.	Lung volumes are low compared to the previous study. Left-sided aortic device is noted with single lead terminating in unchanged position in the right ventricle. Heart size appears at least mildly enlarged. The mediastinal and hilar contours are unremarkable. There is crowding of the bronchovascular structures without overt pulmonary edema. Streaky opacities in the lung bases likely reflect areas of atelectasis. No pleural effusion or pneumothorax is present. There are no acute osseous abnormalities.

Figure 3. Qualitative results on the MIMIC-CXR dataset. Matches with the ground truth are highlighted in the same colors, while inconsistencies are marked in black.

aligning vision and language in the medical domain. The image size is set to 224, with feature channels of 768 for LRP and GRP and a fixed hyperbolic mapping channel of 512. The coefficients α and β are empirically set to 2 and 0.5, respectively. Optimization is performed using the AdamW optimizer with a weight decay of 0.05, an initial learning rate of $5e-5$, and a cosine learning rate schedule. Training runs for 6 epochs with a batch size of 18. All experiments are conducted on an NVIDIA A800 GPU (80GB) for about 10 hours using Python 3.10, PyTorch 2.4.0, and Ubuntu 22.04.

Baseline. We build a strong baseline by replacing CLIP with the MedKLIP foundation model from [13] to incorporate medical domain knowledge. All our experiments are conducted on this baseline unless otherwise specified.

4.2. Comparison with State-of-the-art Methods

Quantitative Results. To verify the effectiveness of our model, we compare its performance against various state-of-the-art (SOTA) models, including R2Gen [4], M2TR [22], MKSG [37], CliBert [36], CVT2Dis. [21], M2KT [38], ME [34], KiUT [11], DCL [15], RGRG [28], UAR [16], HERGen [30], PromptMRG [13], and EKAGen [2]. Detailed comparison results on the MIMIC-CXR and IU X-Ray datasets are presented in Table 1 and Table 2, re-

spectively. For the MIMIC-CXR dataset, as shown in Table 1, our proposed method achieves SOTA performance across all evaluation metrics, consistently outperforming the second-best approach by a large margin. Concretely, our method obtains the absolute improvements of 4.6%, 6.0%, 6.5%, 6.3%, 4.2%, and 4.9% over the recent work EKAGen on various NLG metrics. In terms of the CE metrics, our method outperforms the second-best EKAGen by 11.1%, 13.0%, and 9.3% in Precision, Recall, and F1, respectively. For the IU X-Ray dataset, we follow PromptMRG [13] to evaluate on the entire dataset using pre-trained models from the MIMIC-CXR dataset. As illustrated in Table 2, our method achieves either the highest or runner-up performance across all NLG metrics and the highest performance on all CE metrics, surpassing the second-best model by 1.2% and 6.3% in the mean NLG and CE metrics, respectively. Overall, our model consistently outperforms the second-best method, achieving the average improvement of 7.4% and 2.9% across all evaluation metrics on the MIMIC-CXR and IU X-Ray datasets, respectively.

Qualitative Results. Figure 3 presents two qualitative examples that highlight the superiority of our REVTA model over both the baseline and the PromptMRG SOTA method. In Figure 3, text segments that completely align with the

Setting	LRE	FVTAF	NLG Metrics						CE Metrics			Avg
			BLEU-1	BLEU-2	BLEU-3	BLEU-4	METEOR	ROUGE	Precision	Recall	F1	
Baseline			0.432	0.283	0.210	0.159	0.177	0.311	0.597	0.586	0.562	0.369
(a)	✓		0.453	0.312	0.224	0.178	0.186	0.325	0.612	0.590	0.571	0.384
(b)		✓	0.457	0.296	0.228	0.175	0.186	0.329	0.607	0.595	0.571	0.383
(c)	✓	✓	0.465	0.318	0.235	0.182	0.199	0.336	0.628	0.613	0.592	0.397

Table 3. Analysis on the effectiveness of each component on MIMIC-CXR test set.

LLMs	Time (s)	NLG Metrics						CE Metrics			Avg
		BLEU-1	BLEU-2	BLEU-3	BLEU-4	METEOR	ROUGE	Precision	Recall	F1	
GPT-4	15.02	0.286	0.131	0.048	0.00	0.117	0.187	0.293	0.229	0.247	0.192
GPT-4o	8.77	0.326	0.159	0.081	0.047	0.115	0.188	0.146	0.219	0.166	0.161
GPT-4o-mini	7.50	0.254	0.104	0.045	0.022	0.104	0.161	0.063	0.083	0.067	0.100
GPT-4.5	18.72	0.306	0.140	0.073	0.045	0.112	0.182	0.303	0.224	0.233	0.180
Ours	3.36	0.379	0.236	0.161	0.119	0.150	0.266	0.466	0.766	0.581	0.347

Table 4. Comparison with GPT series multimodal LLMs on randomly sampled MIMIC-CXR test set.

ground truth are highlighted in same colors, whereas non-corresponding segments are shown in black. As observed, our model effectively captures most of the key descriptions found in the ground truth. Specifically, it accurately identifies critical disease labels such as enlarged cardiomeastinum, pleural effusion, pneumothorax, as well as pertinent past medical history. In contrast, PromptMRG fails to accurately capture the past medical history and lung status, while the baseline generates several irrelevant details. Notably, our proposed method successfully eliminates these irrelevant sentences and produces more precise expressions, demonstrating the effectiveness of our approach.

4.3. Ablation Study

Effectiveness of Each Component. We assess the effectiveness of each component in our method using the MIMIC-CXR dataset by incrementally incorporating them. The experimental results, summarized in Table 3, demonstrate that integrating the LRE module improves the baseline performance by 1.8% and 0.9% in average NLG and CE metrics, respectively, validating the advantage of adaptively retrieving the most relevant GRPs for report generation. Similarly, the FVTAF module alone achieves gains of 1.7% and 0.9% over the baseline in mean NLG and CE metrics, respectively, emphasizing the effectiveness of fine-grained alignment and fusion. When combining both the LRE and FVTAF modules, our REVTAf framework achieves significant improvements of 2.7% and 2.9% over the baseline in mean NLG and CE metrics, underscoring the critical role of these components in enhancing radiology report generation. The proposed approach achieves an overall improvement of 2.8% across all evaluation metrics compared to the baseline.

Comparison Results with multimodal LLMs. To validate the effectiveness of our method in radiology report generation, we compare it with mainstream multimodal LLMs, including GPT-4, GPT-4o, GPT-4o-mini, and GPT-4.5, using 16 randomly selected samples from the MIMIC-CXR test set (Table 4). For each sample, we measure report generation performance and inference time, averaging the results for comparison. Our method consistently outperforms GPT-series multimodal LLMs across all metrics while being more efficient, making it better suited for clinical use. In contrast, GPT models, despite their extensive training, struggle with medical-specific knowledge, resulting in poorer performance and longer inference times. Among the GPT-4 series, smaller models (GPT-4o and GPT-4o-mini) underperform compared to larger ones (GPT-4 and GPT-4.5). While GPT-4o and GPT-4.5 slightly surpass GPT-4 in language metrics, they lag in diagnostic accuracy. Overall, GPT-4 performs best among these models but remains significantly inferior to our method.

5. Conclusion

We propose the Retrieval Enhanced Visual-Text Alignment and Fusion (REVTAf) framework for radiology report generation. REVTAf features a Learnable Retrieval Enhancer (LRE) to adaptively retrieve the most relevant GRPs, enhancing visual representations, especially for tail classes. Additionally, it employs a Fine-grained Visual-Text Alignment and Fusion (FVTAF) strategy, incorporating an FCC constraint for precise alignment and optimal transport-based cross-attention mechanism for improved fusion under weak supervision. Experiments show that REVTAf achieves favorable performance, delivering gains of 7.4% and 2.9% on the MIMIC-CXR and IU X-Ray datasets, significantly outperforming mainstream multimodal LLMs.

Acknowledgements

This study was supported under the Key Research and development Project of Yunnan Province (Grant No. 202402AD080006). It was also funded by the National Science Foundation of China (Grant No. 62201341).

References

- [1] Peter Anderson, Xiaodong He, Chris Buehler, Damien Teney, Mark Johnson, Stephen Gould, and Lei Zhang. Bottom-up and top-down attention for image captioning and visual question answering. In *Proceedings of the IEEE conference on computer vision and pattern recognition*, pages 6077–6086, 2018. 2
- [2] Shenshen Bu, Taiji Li, Yuedong Yang, and Zhiming Dai. Instance-level expert knowledge and aggregate discriminative attention for radiology report generation. In *Proceedings of the IEEE/CVF Conference on Computer Vision and Pattern Recognition*, pages 14194–14204, 2024. 2, 7
- [3] Wenting Chen, Xiang Li, Linlin Shen, and Yixuan Yuan. Fine-grained image-text alignment in medical imaging enables cyclic image-report generation. *arXiv preprint arXiv:2312.08078*, 2023. 3, 4
- [4] Zhihong Chen, Yan Song, Tsung-Hui Chang, and Xiang Wan. Generating radiology reports via memory-driven transformer. *arXiv preprint arXiv:2010.16056*, 2020. 2, 7
- [5] Zhihong Chen, Yaling Shen, Yan Song, and Xiang Wan. Cross-modal memory networks for radiology report generation. *arXiv preprint arXiv:2204.13258*, 2022. 2, 6
- [6] Marcella Cornia, Matteo Stefanini, Lorenzo Baraldi, and Rita Cucchiara. Meshed-memory transformer for image captioning. In *Proceedings of the IEEE/CVF conference on computer vision and pattern recognition*, pages 10578–10587, 2020. 1, 2
- [7] Bo Dai, Sanja Fidler, Raquel Urtasun, and Dahua Lin. Towards diverse and natural image descriptions via a conditional gan. In *Proceedings of the IEEE international conference on computer vision*, pages 2970–2979, 2017. 2
- [8] Michael Denkowski and Alon Lavie. Meteor 1.3: Automatic metric for reliable optimization and evaluation of machine translation systems. In *Proceedings of the sixth workshop on statistical machine translation*, pages 85–91, 2011. 6
- [9] Alex Graves and Alex Graves. Long short-term memory. *Supervised sequence labelling with recurrent neural networks*, pages 37–45, 2012. 2
- [10] Xiaowei Hu, Zhe Gan, Jianfeng Wang, Zhengyuan Yang, Zicheng Liu, Yumao Lu, and Lijuan Wang. Scaling up vision-language pre-training for image captioning. In *Proceedings of the IEEE/CVF conference on computer vision and pattern recognition*, pages 17980–17989, 2022. 2
- [11] Zhongzhen Huang, Xiaofan Zhang, and Shaoting Zhang. Kiut: Knowledge-injected u-transformer for radiology report generation. In *Proceedings of the IEEE/CVF Conference on Computer Vision and Pattern Recognition*, pages 19809–19818, 2023. 2, 6, 7
- [12] Jeremy Irvin, Pranav Rajpurkar, Michael Ko, Yifan Yu, Silvana Ciurea-Ilcus, Chris Chute, Henrik Marklund, Behzad Haghighi, Robyn Ball, Katie Shpanskaya, et al. Chexpert: A large chest radiograph dataset with uncertainty labels and expert comparison. In *Proceedings of the AAAI conference on artificial intelligence*, pages 590–597, 2019. 1, 6
- [13] Haibo Jin, Haoxuan Che, Yi Lin, and Hao Chen. Promptmrg: Diagnosis-driven prompts for medical report generation. In *Proceedings of the AAAI Conference on Artificial Intelligence*, pages 2607–2615, 2024. 1, 2, 3, 4, 6, 7
- [14] Haoran Li, Chun-Mei Feng, Yong Xu, Tao Zhou, Lina Yao, and Xiaojun Chang. Zero-shot camouflaged object detection. *IEEE Transactions on Image Processing*, 2023. 2
- [15] Mingjie Li, Bingqian Lin, Zicong Chen, Haokun Lin, Xiaodan Liang, and Xiaojun Chang. Dynamic graph enhanced contrastive learning for chest x-ray report generation. In *Proceedings of the IEEE/CVF Conference on Computer Vision and Pattern Recognition*, pages 3334–3343, 2023. 2, 7
- [16] Yaowei Li, Bang Yang, Xuxin Cheng, Zhihong Zhu, Hongxiang Li, and Yuexian Zou. Unify, align and refine: Multi-level semantic alignment for radiology report generation. In *Proceedings of the IEEE/CVF international conference on computer vision*, pages 2863–2874, 2023. 1, 7
- [17] Chin-Yew Lin. Rouge: A package for automatic evaluation of summaries. In *Text summarization branches out*, pages 74–81, 2004. 6
- [18] Fenglin Liu, Xian Wu, Shen Ge, Wei Fan, and Yuexian Zou. Exploring and distilling posterior and prior knowledge for radiology report generation. In *Proceedings of the IEEE/CVF conference on computer vision and pattern recognition*, pages 13753–13762, 2021. 1, 2
- [19] Shilong Liu, Zhaoyang Zeng, Tianhe Ren, Feng Li, Hao Zhang, Jie Yang, Qing Jiang, Chunyuan Li, Jianwei Yang, Hang Su, Jun Zhu, and Lei Zhang. Grounding dino: Marrying dino with grounded pre-training for open-set object detection, 2024. 5
- [20] Jiasen Lu, Caiming Xiong, Devi Parikh, and Richard Socher. Knowing when to look: Adaptive attention via a visual sentinel for image captioning. In *Proceedings of the IEEE conference on computer vision and pattern recognition*, pages 375–383, 2017. 2
- [21] Aaron Nicolson, Jason Dowling, and Bevan Koopman. Improving chest x-ray report generation by leveraging warm starting. *Artificial intelligence in medicine*, 144:102633, 2023. 7
- [22] Farhad Nooralahzadeh, Nicolas Perez Gonzalez, Thomas Frauenfelder, Koji Fujimoto, and Michael Krauthammer. Progressive transformer-based generation of radiology reports. *arXiv preprint arXiv:2102.09777*, 2021. 7
- [23] K O’Shea. An introduction to convolutional neural networks. *arXiv preprint arXiv:1511.08458*, 2015. 2
- [24] Yingwei Pan, Ting Yao, Yehao Li, and Tao Mei. X-linear attention networks for image captioning. In *Proceedings of the IEEE/CVF conference on computer vision and pattern recognition*, pages 10971–10980, 2020. 1, 2
- [25] Kishore Papineni, Salim Roukos, Todd Ward, and Wei-Jing Zhu. Bleu: a method for automatic evaluation of machine

- translation. In *Proceedings of the 40th annual meeting of the Association for Computational Linguistics*, pages 311–318, 2002. [6](#)
- [26] Steven J Rennie, Etienne Marcheret, Youssef Mroueh, Jerret Ross, and Vaibhava Goel. Self-critical sequence training for image captioning. In *Proceedings of the IEEE conference on computer vision and pattern recognition*, pages 7008–7024, 2017. [2](#)
- [27] Akshay Smit, Saahil Jain, Pranav Rajpurkar, Anuj Pareek, Andrew Y Ng, and Matthew P Lungren. Chexbert: combining automatic labelers and expert annotations for accurate radiology report labeling using bert. *arXiv preprint arXiv:2004.09167*, 2020. [4](#)
- [28] Tim Tanida, Philip Müller, Georgios Kaissis, and Daniel Rueckert. Interactive and explainable region-guided radiology report generation. In *Proceedings of the IEEE/CVF Conference on Computer Vision and Pattern Recognition*, pages 7433–7442, 2023. [7](#)
- [29] A Vaswani. Attention is all you need. *Advances in Neural Information Processing Systems*, 2017. [2](#)
- [30] Fuying Wang, Shenghui Du, and Lequan Yu. Hergen: Elevating radiology report generation with longitudinal data, 2024. [7](#)
- [31] Jun Wang, Abhir Bhalerao, and Yulan He. Cross-modal prototype driven network for radiology report generation. In *European Conference on Computer Vision*, pages 563–579. Springer, 2022. [2](#)
- [32] Shuang Wang, Qiaoling Lin, Xiutiao Ye, Yu Liao, Dou Quan, Zhongqian Jin, Biao Hou, and Licheng Jiao. Multi-view feature fusion and visual prompt for remote sensing image captioning. *IEEE Transactions on Geoscience and Remote Sensing*, 2024. [1](#), [5](#)
- [33] Zifeng Wang, Zhenbang Wu, Dinesh Agarwal, and Jimeng Sun. Medclip: Contrastive learning from unpaired medical images and text, 2022. [2](#)
- [34] Zhanyu Wang, Lingqiao Liu, Lei Wang, and Luping Zhou. Metransformer: Radiology report generation by transformer with multiple learnable expert tokens. In *Proceedings of the IEEE/CVF Conference on Computer Vision and Pattern Recognition*, pages 11558–11567, 2023. [2](#), [7](#)
- [35] Chaoyi Wu, Xiaoman Zhang, Ya Zhang, Yanfeng Wang, and Weidi Xie. Medklip: Medical knowledge enhanced language-image pre-training in radiology, 2023. [2](#), [6](#)
- [36] Bin Yan and Mingtao Pei. Clinical-bert: Vision-language pre-training for radiograph diagnosis and reports generation. In *Proceedings of the AAAI Conference on Artificial Intelligence*, pages 2982–2990, 2022. [2](#), [7](#)
- [37] Shuxin Yang, Xian Wu, Shen Ge, S Kevin Zhou, and Li Xiao. Knowledge matters: Chest radiology report generation with general and specific knowledge. *Medical image analysis*, 80:102510, 2022. [7](#)
- [38] Shuxin Yang, Xian Wu, Shen Ge, Zhuozhao Zheng, S Kevin Zhou, and Li Xiao. Radiology report generation with a learned knowledge base and multi-modal alignment. *Medical Image Analysis*, 86:102798, 2023. [7](#)
- [39] Yifei Yang, Wonjun Lee, Dongmian Zou, and Gilad Lerman. Improving hyperbolic representations via gromov-wasserstein regularization. In *European Conference on Computer Vision*, pages 211–227. Springer, 2024. [4](#)
- [40] Jong Chul Ye, Yujin Oh, et al. Otseg: Multi-prompt sinkhorn attention for zero-shot semantic segmentation. In *The 18th European Conference on Computer Vision, ECCV 2024*. European Computer Vision Association (ECVA), 2024. [5](#)
- [41] Jiahui Yu, Zirui Wang, Vijay Vasudevan, Legg Yeung, Mojtaba Seyedhosseini, and Yonghui Wu. Coca: Contrastive captioners are image-text foundation models. *arXiv preprint arXiv:2205.01917*, 2022. [1](#), [2](#)
- [42] Ke Yu, Shantanu Ghosh, Zhexiong Liu, Christopher Deible, and Kayhan Batmanghelich. Anatomy-guided weakly-supervised abnormality localization in chest x-rays. In *International Conference on Medical Image Computing and Computer-Assisted Intervention*, pages 658–668. Springer, 2022. [3](#)
- [43] Zhenyu Zhang, Benlu Wang, Weijie Liang, Yizhi Li, Xuechen Guo, Guanhong Wang, Shiyang Li, and Gaoang Wang. Sam-guided enhanced fine-grained encoding with mixed semantic learning for medical image captioning. In *ICASSP 2024-2024 IEEE International Conference on Acoustics, Speech and Signal Processing (ICASSP)*, pages 1731–1735. IEEE, 2024. [1](#)